EUROPEAN ORGANIZATION FOR NUCLEAR RESEARCH

CERN-SPSC/89-43
SPSC/P238Add.1
16 August 1989

Addendum to Proposal P238:

MEASUREMENT OF B_s MIXING

A. Brandt, S. Erhan, D. Lynn, M. Medinnis, P. Schlein*, J. Zweizig
University of California, Los Angeles, U.S.A.

T. Ypsilantis
College de France[1], Paris, France

G. Borreani
University of Ferrara and INFN[2], Italy

A. Kaschuk, V. Samsonov, V. Sarantzev, E. Spiridenkov, A. Vorobyov
Institute for Nuclear Physics, Gatchina, Leningrad, U.S.S.R.

M. Calvetti
University of Perugia and INFN[2], Italy

J.B. Cheze, J. Zsembery
Centre d'Etudes Nucleaires – Saclay[3], Gif-sur-Yvette, France

R. Dzhelyadin, Y. Guz, V. Kubic, V. Obraztsov, A. Ostankov
IHEP-Serpukhov, Protvino, U.S.S.R.

C. Biino, R. Cester, A. Migliori, R. Mussa, S. Palestini
University of Torino and INFN[2], Italy

ABSTRACT

We report the results of a detailed investigation into the capability of our proposed forward B-spectrometer experiment to observe and measure the time oscillations in the decay of tagged B_s mesons. With the best conceivable electromagnetic calorimeter resolution ($0.5\%/\sqrt{E}$ for Liquid Xenon) and with both outgoing collider arms instrumented, 9000 reconstructed B_s are obtainable per 10 $pbarn^{-1}$ integrated luminosity. Lead-Glass calorimetry with $4\%/\sqrt{E}$ leads to 6000 events. Charged kaons are shown to tag 58% of these events with an adequate (good tag/all tag) ratio of 73%. Using Lead-Glass calorimetry with only one instrumented arm, $\Delta M/\Gamma$ would be measured with 3000 events, for values up to 15 or more, with an error of about ± 0.1. Our conclusion is that superior mixing measurements can be performed with the proposed apparatus.

---

*) Spokesman
[1]) Pending approval of the Laboratory and IN2P3
[2]) Pending approval of INFN
[3]) Pending approval of CEN-Saclay

TABLE OF CONTENTS

1. INTRODUCTION

The Forward Beauty Spectrometer in proposal P238 has the following properties:

- Real-time vertex calculations based on silicon micro-vertex detector data yield the suppression of minimum bias background necessary for efficient triggering on beauty particles.

- The average momentum of detected and reconstructed B-mesons is about 35 Gev/c and the B proper time can be measured with a precision better than $\sigma_t/t = 6\%$. These facts allow excellent B-$\bar{B}$ oscillation studies to be made.

- Particle identification is furnished offline with a system of liquid and gas Ring Imaging Cerenkov Counters.

- The forward peaking of heavy flavor particles should be even more pronounced at the higher energy UNK, LHC and SSC colliders. Thus, our proposed experiment would be a first example of an important class of future beauty experiments which should eventually allow an effective search for CP violation in B decay.

In document P238, we presented details of the trigger design and detector which would furnish more than 2×10^5 reconstructed B-Mesons per 10 pbarn^{-1} integrated luminosity at the CERN SPS-Collider with $\sqrt{s}$ = 630 GeV.

In the present Addendum to P238, we examine in detail the suitability of our proposed experiment for a measurement of B_s-$\bar{B}_s$ oscillations. We find a capability which is superior to that of any other existing or proposed experiment.

Chapter 2 contains a discussion of the relevant mixing formalism. Chapter 3 contains a discussion of the acceptance properties of the proposed apparatus, a performance summary of the trigger and the reconstruction efficiencies for B_s mesons. The expected yields are given.

Chapter 4 contains the results of a Monte-Carlo study of flavor tagging procedures in which it is shown that charged kaons can be used to tag 58% of all reconstructed B_s mesons. The B_s lifetime measurement is described in Chapter 5. In Chapter 6 we present mixing analyses of simulated Monte-Carlo data samples, which would result from runs with integrated luminosity of 10 pbarn^{-1}, and define the minimum hardware capabilities necessary for a satisfactory measurement with a reasonable "margin of safety".

In Chapter 7 we discuss, as best we can with the available information, the apparent capabilities of other existing or planned beauty experiments to measure B_s-mixing.

We conclude that superior mixing measurements can be performed with the proposed apparatus at the SPS-Collider.

2. THE OBSERVATION OF B_s MIXING

Four proper time distributions will be obtained from the reconstructed and tagged B_s and $\bar{B}_s$ mesons:

$$t^+ \; B_s(t) \tag{1}$$

$$t^- \; B_s(t) \tag{2}$$

$$t^+ \; \bar{B}_s(t) \tag{3}$$

$$t^- \; \bar{B}_s(t) \tag{4}$$

where t^+ and t^- denote the two charges of the possible tagging particles (e.g., e^+, e^-, μ^+, μ^-, K^+, K^-). We note that, since a B_s can be produced together with a $\bar{B}_u$, $\bar{B}_d$ or $\bar{B}_s$, a tagging particle can arise from any one of these. The latter two states are themselves subject to oscillation and can lead to the wrong sign tag, refered to in this document as "mistagging". Other sources of mistagging are, for example, background under the B_s signal, other physics sources of the tagging particles, etc. Tagging procedures are discussed in Chapter 4 in some detail.

In order to arrive at the equations which describe the above four distributions (ignoring the possibility of CP violation), we start by expressing B^0 and $\bar{B}^0$ as the usual linear combination of mass eigenstates, B_1 and B_2:

$$|B^0> \; = [|B_1> \; + \; |B_2>] \; / \; \sqrt{2} \tag{5}$$

$$|\bar{B}^0> \; = [|B_1> \; - \; |B_2>] \; / \; \sqrt{2} \tag{6}$$

With the $B^0 \leftrightarrow \bar{B}^0$ transitions allowed by the second-order weak interaction (box diagram), we have as the time-evolved state for an initial B^0:

$$\psi(t) = [e^{-iM_1t-\Gamma_1t/2} \cdot |B_1> \; + \; e^{-iM_2t-\Gamma_2t/2} \cdot |B_2>] \; / \; \sqrt{2} \tag{7}$$

Expanding $|B_1>$ and $|B_2>$ in terms of the observed $|B^0>$ and $|\bar{B}^0>$ states, and projecting out their amplitudes, we have as the probabilities to see B^0 and $\bar{B}^0$:

$$|<B^0|\psi(t)>|^2 \; = e^{-\Gamma t} \cdot [1 \; + \; \cos(\Delta M t)] \; / \; 2 \tag{8}$$

$$|<\bar{B}^0|\psi(t)>|^2 \; = e^{-\Gamma t} \cdot [1 \; - \; \cos(\Delta M t)] \; / \; 2 \tag{9}$$

We write in (8) and (9), $\Gamma \equiv \Gamma_1 \; = \; \Gamma_2$, because of the large phase space available in B decay, and $\Delta M \; = \; M_1 - M_2$. As required, the sum of equations (8) and (9), $e^{-\Gamma t}$, describes the untagged B_s decay.

Integrating Eqs. 8 and 9 over time, we find that the rates for no-oscillation and oscillation, respectively, go as $(2+x^2)/(1+x^2)$ and $x^2/(1+x^2)$, where $x \equiv \Delta M/\Gamma$. If we assume, as is reasonable, that a B_s and its accompanying $\bar{B}$ decay independently and that we only measure the time dependence of the B_s, then the correct expressions to describe the tagged time distributions in Eqs. 1-4 are just Eqs. 8 and 9 multiplied by the appropriate time-averaged rate. These are shown in Table 1 for the four cases of Eqs. 1-4 and for the two possible initial states.

Krawczyk et al. (DESY 88-16) have pointed out that if data in Reactions 2 and 3 (or Reactions 1 and 4) are added together, the time dependences, $[1 \pm \cos(\Delta M t)/(1+x^2)]$, result. This can be seen to be the case from the relations in Table 1, independently for each of the two possible initial states. What we can see in addition, however, is that, if the initial states, $B\bar{B}_s$ and $\bar{B}B_s$ occur with equal probability, this occurs independently for each of Reactions 1-4, as shown in column 4 of Table 1.

Table 1: *Joint Time-Integrated, Time-Dependent Rates(a,b,c)*

Final State	Initial State $B\bar{B}_s$	Initial State $\bar{B}B_s$	Equal Sum
$t^+ B_s(t)$	$(2+x^2)\cdot[1-\cos]$	$x^2\cdot[1+\cos]$	$1-[1/(1+x^2)]\cdot\cos$
$t^- B_s(t)$	$x^2\cdot[1-\cos]$	$(2+x^2)\cdot[1+\cos]$	$1+[1/(1+x^2)]\cdot\cos$
$t^+ \bar{B}_s(t)$	$(2+x^2)\cdot[1+\cos]$	$x^2\cdot[1-\cos]$	$1+[1/(1+x^2)]\cdot\cos$
$t^- \bar{B}_s(t)$	$x^2\cdot[1+\cos]$	$(2+x^2)\cdot[1-\cos]$	$1-[1/(1+x^2)]\cdot\cos$

(a) The B decay which provides the tagging particle is time-integrated. The B_s decay is time-dependent. Throughout this table, $x = \Delta M/\Gamma$ for the tagging B

(b) We note that in a B decay, for example, a μ^+ or a K^+ tag results (if the K results from the $\bar{c} \to \bar{s}$ transition). In a tagging $\bar{B}$ decay, of course, the signs are opposite.

(c) To simplify the reading of this table, a common factor $e^{-\Gamma t}/(1+x^2)$ is suppressed in all terms in columns 2 and 3, as is the argument, (ΔMt), from all cosine functions.

Thus the distributions for the four Reactions must be pairwise identical if valence quarks do not play a role in modifying the equality of the initial states (presumably the case for production of B_s at small Feynman-x).

It remains to be pointed out, as in Krawczyk et al., that since the accompanying B (or $\bar{B}$), which provides the tagging particle, can be either B_u, B_d or B_s, the factor $[1/(1+x^2)]$ in the relations in the last column of Table 1 must be weighted over the three types of tag-producing B's according to their relative production frequency. In calculating the weighted average of $[1/(1+x^2)$ over B_u (40%), B_d (40%) and B_s (20%), x is taken to be 0, 0.7 and 15, respectively.

The resulting constant, $K = 0.67$, is essentially a "dilution" factor since it decreases the amplitude of the oscillation from the value it would have were the flavor of the decaying B always correctly determined. For example, the observed distribution from, for example the $t^+ B_s(t)$ final state, now has the form: $1 - K\cos(\Delta Mt)$. Other contributions to dilution come from mistagging or background (the tagging problem is discussed in detail in Chapter 4). For example, if the tag used is only 70% efficient (good/all = 70%), then K receives another multiplicative contribution of (good − bad)/all = 0.4. The effective value of the constant, K, is discussed in Chapter 6, where we present the complete analysis of simulated data samples.

3. YIELDS OF RECONSTRUCTED B_s AND $\bar{B}_s$ MESONS

Most of the ingredients for a realistic estimate for B_s yields can be found in Proposal P238. See, for example, Section 8.1 (page 54). Here we list, in Table 2, the various steps which result in an estimate of 4500 reconstructed B_s and 4500 reconstructed $\bar{B}_s$ mesons per 10 pbarn^{-1} integrated luminosity. We note that these numbers represent the "ultimate capability" of the SPS-Collider, namely if both outgoing arms are instrumented and if the best conceivable electromagnetic calorimeter is used (Liquid-Xenon). As is discussed below, while maximum statistics and minimal background are clearly always desirable features, a proper measurement of B_s mixing can be made with less than this maximum commitment. The following two sections explain the various steps in arriving at the estimates.

Table 2: B_s & $\bar{B}_s$ Event Yields(*)

10^8 $b\bar{b}$ Produced for $\int \mathcal{L} dt$ = 10 pbarn^{-1}

2.0×10^7 B_s	2.0×10^7 $\bar{B}_s$	0.20 = B_s Production
6.0×10^6	6.0×10^6	0.30 = 2-Arm Geometrical Acceptance
3.0×10^5	3.0×10^5	0.05 = BR($B_s \rightarrow D_s^* n\pi\pm$)
3.0×10^5	3.0×10^5	1.00 = BR($D_s^* \rightarrow D_s \gamma$)
4.4×10^4	4.4×10^4	0.15 = BR($D_s \rightarrow KK\pi$, $KK3\pi$, K^0K)
3.0×10^4	3.0×10^4	0.68 = No Other Interaction in Bunch Crossing
2.8×10^4	2.8×10^4	0.94 = Vertex Acceptance of Silicon μVertex
1.18×10^4	1.18×10^4	0.42 = Trigger Efficiency (D_s^* 3π)
1.05×10^4	1.05×10^4	0.89 = Track Finding Efficiency
4500 B_s	4500 $\bar{B}_s$	0.43 = Event Reconstruction This assumes best e.m. calorimetry. See text for further discussion.

(*) The cuts in this table are discussed in Section 3.1

3.1 Geometric Acceptance, Branching Ratios & Trigger Efficiencies

As in P238, we base our yield estimates on an assumed integrated luminosity, $\int \mathcal{L} dt = 10$ pbarn^{-1}, and a $b\bar{b}$ total cross section of 10 μbarn. These assumptions correspond to a $b\bar{b}$ production sample of 10^8 events. The following losses and efficiencies are tabulated in Table 2:

- A $\bar{b}$-quark is assumed to have a 20% probability of combining with an s-quark to make a B_s-meson. This leads to 2×10^7 B_s and 2×10^7 $\bar{B}_s$ mesons produced, with negligible simultaneous production.

- Geometric Acceptance – According to PYTHIA (which assumes $b\bar{b}$ production via gluon-gluon fusion and quark-quark fusion), the decay products of 30% of all produced B_s mesons are fully contained by a system of two 600 mrad aperture forward spectrometers. This leads to 6.0×10^6 B_s and 6.0×10^6 $\bar{B}_s$ produced and fully contained in the aperture (these numbers are slightly smaller than the 6.4×10^6 given on page 55 of P238, due to a recalculation of the geometrical acceptance for the specific B_s decay mode discussed below).

- B_s Branching Ratios – We assume BR = 5% for the total of all reactions of the type:

$$B_s \rightarrow D_s^* + n\pi\pm$$

This leads to 3.0×10^5 B_s (and the same number of $\bar{B}_s$) with these decay modes. We noted in Table 7, page 56 of P238 that the observed ARGUS BR = 6.7% for reactions of the type $B_d \rightarrow D^* + n\pi$ with n = 1,2,3. It seems likely that we shall also be able to reconstruct such final states with n > 3 and that, therefore, our effective useful BR will be larger than the 5% assumed.

- D_s^* Branching Ratio – We assume that all D_s^* decay via the mode:

$$D_s^* \rightarrow D_s \gamma$$

This has the consequence that an electromagnetic calorimeter is essential for this experiment. The characteristics of the calorimetry required for the effective reconstruction of these events are discussed in the following section. (Note that with such calorimetry, we also acquire the capability to detect $D^{*0} \rightarrow D^0\gamma$ (BR = 48%) and gain additional efficiency for charged D^* in $D^{*+} \rightarrow D^+\gamma$ (BR = 17%)).

- $D_s\pm$ Branching Ratio – We take BR = 15% for all known charged final states ($K^+K^-\pi\pm$, K^+K^- 3π, $K^0K\pm$). This reduces each sample to 44,250 events.

- Pileup loss – As in P238 (see page 55 and Section 3.2), 68% of all B_s events have no second inelastic interaction in the same bunch crossing at an average luminosity of 2×10^{30} cm^{-2} sec^{-1}. For purposes of the present estimates, we assume that all events in bunch crossings which contain more than one inelastic interaction will be lost (in practice, however, since many of multiple interaction bunchs may be usable, 68% is a conservative estimate of this efficiency). The B_s sample is reduced to 30,090 events.

- Vertex Acceptance in Silicon – About 6% of events have vertices outside the acceptance range in longitudinal coordinate, z, of the silicon micro-vertex detector (see Appendix B) and are therefore lost. The samples are thus reduced to 27,682 events each.

- Trigger Efficiency – The trigger simulation is discussed in detail in Chapter 4 of P238 with some results given in Chapter 7. For the present estimates, we have focussed our attention on one particular final state:

$$B_s \rightarrow D_s^* \pi\pi\pi$$
$$\hookrightarrow D_s \gamma$$
$$\hookrightarrow \phi\pi$$
$$\hookrightarrow K^+K^- \qquad (10)$$

We calculate a trigger efficiency of 42% for this state. This may be compared with the results given in Table 6 (page 51) of P238 of 47% for $B_d \rightarrow D^*\pi\pi\pi$ (8 tracks) and 41% for $D^0\pi\pi$ (6 tracks). The samples are thus reduced to 11,627 each.

- Track Finding Efficiency – We assume a 98% track finding efficiency and therefore $(.98)^n$ for the entire event. For the above 6-track event, this efficiency is 88.6%, which reduces each sample to 10,301 events.

- Reconstruction Efficiency – An efficiency of 43% follows from the analysis discussed in the following section when an electromagnetic calorimeter with resolution $\sigma_E/E = 0.5\%/\sqrt{E}$ is used (Liquid-Xenon, as discussed in Appendix D of P238). 43% is somewhat larger than the 36% reported for the decay $B \rightarrow D^*3\pi$ in P238 (page 51), because of some improvements in reconstruction software. For other calorimeters (Lead-Glass, etc.), the reconstruction efficiency is smaller, as discussed in the following section.

3.2 B_S Reconstruction: Signal & Background Estimates

Chapter 7 of the P238 proposal discussed the B-meson reconstruction procedure and combinatoric background problem in some detail. The present analysis of the $D_s^* \rightarrow D_s\gamma$ reaction requires the introduction of a new factor, namely the effect of using electromagnetic calorimeter information in the B_s-meson reconstruction. We have thus studied the effect of calorimeter energy and spatial resolutions on both the reconstruction yield and the B_s signal/background ratio.

Following the procedures outlined in Chapter 7 of P238, we construct the invariant mass difference, $M(D_s^*) - M(D_s)$ for the B_s decay in Reaction 10. We plot the resulting mass difference distributions in Fig. 1 for 12 combinations of calorimeter parameters. Calorimeter energy resolutions of 0.5%, 1%, 2% and 4% and spatial resolutions of 0.3 mm, 1.0 mm and 10 mm are considered. In constructing these plots, we randomly vary all charged track and γ parameters in accordance with the expected energy and angular resolutions. Since the purpose of these plots is to demonstrate the effect of different calorimeter resolutions on the invariant mass resolution, we do not include the combinatoric background resulting from all possible track combinations – only the correct B_s decay tracks are used.

Although there is very little dependence of the invariant mass difference resolution on calorimeter spatial resolution seen in Fig. 1, there is a very large dependence on its energy resolution. For the $0.5\%/\sqrt{E}$ calorimeter (e.g.: the Liquid-Xenon device discussed in Appendix D of P238), the FWHM is 2 MeV, while for $4\%/\sqrt{E}$ (Lead-Glass), the FWHM is increased to about 12 MeV. As will be demonstrated below, the effect of this poorer resolution is to allow more combinatoric background into the signal region and also to lose some signal because some of the tails in the $M(D_s^*) - M(D_s)$ distribution will be cut off. In addition, a larger fraction of the γ's from D^*'s combine with other γ's in the event to form a π^0 mass; these are then cut out in our selection procedure.

Using appropriate mass cuts in Figs. 1 to select most of the signal peaks leads to the B_s invariant mass distributions shown in Figs. 2 for the same sets of calorimeter parameters. Although there is a significant dependence of the mass resolution on calorimeter parameters, the dependence is weak, due to the fact that, in general, the γ possesses only a small part of the B_s energy (average γ energy is about 1 GeV, compared with average B_s energy of about 35 GeV).

Before discussing the matter of how the signal/background depends on calorimeter resolution, we show in Fig. 3(a) the expected B_s signal for the best calorimeter case ($0.5\%/\sqrt{E}$ and 0.3 mm), with all combinatoric background (obtained as described in Chapter 7 of P238). Fig. 3(b) shows the expected D_s signal with its combinatoric background.

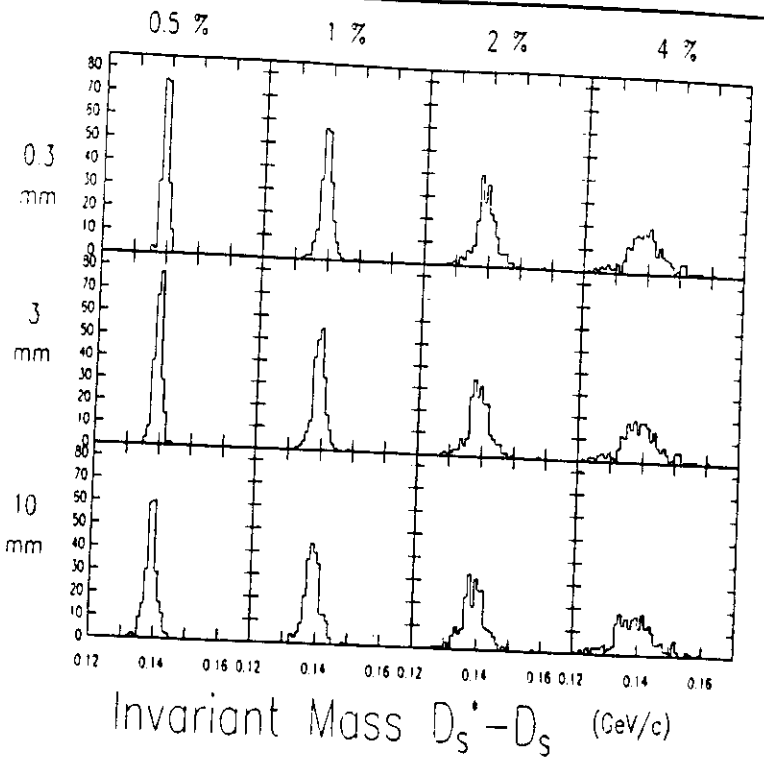

Figure 1: Invariant mass differences, $M(D_s^*) - M(D_s)$, for the indicated 12 combinations of electromagnetic calorimeter energy and spatial resolutions. The spatial resolution is the standard deviation, σ_x. The mass bins are 1 MeV. No combinatoric background is shown. In each case, the energy resolution σ_E/E is the indicated constant (e.g. k = 0.5%) divided by $\sqrt{E}$ in GeV.

The B_s signal size and signal/background have been evaluated for all of the 12 sets of calorimeter resolutions considered (we include the expected background from the general B event sample, in addition to the combinatoric background arising from Reaction 10). Figs. 4(a,b), respectively, contain these results. For the $0.5\%/\sqrt{E}$ calorimeter, the event yield is 9000 total reconstructed B_s and $\bar{B}_s$ events and the signal/background is about 10. The degradations of both these quantities with worsening calorimeter energy resolution are clear. In particular, for a $4\%/\sqrt{E}$ calorimeter (Lead-Glass), the event yield drops to 6000 events and the signal/background to about 4. The question of what calorimeter resolution will allow the extraction of our desired physics results is deferred to Chapter 6 of this document where we give the results of maximum likelihood fits to Monte-Carlo data samples of varying sizes and with varying backgrounds.

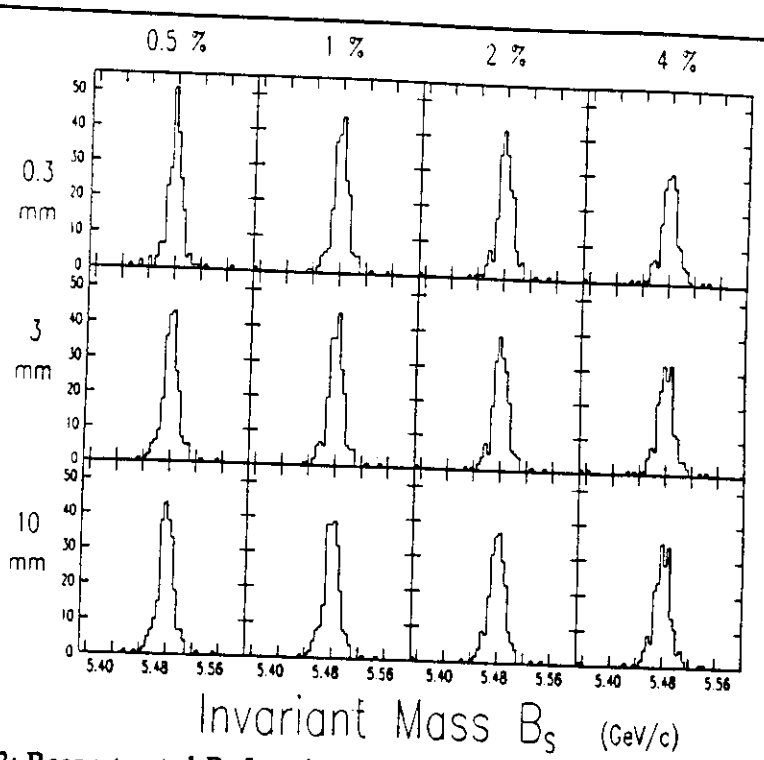

Figure 2: Reconstructed B_s Invariant Mass for the indicated 12 combinations of electromagnetic calorimeter energy and spatial resolutions as in Fig. 1. In each case, an appropriate cut is made on the mass difference, $M(D^*) - M(D_s)$, of the corresponding plot in Fig. 1. The mass bins are 5 MeV. No combinatoric background is shown.

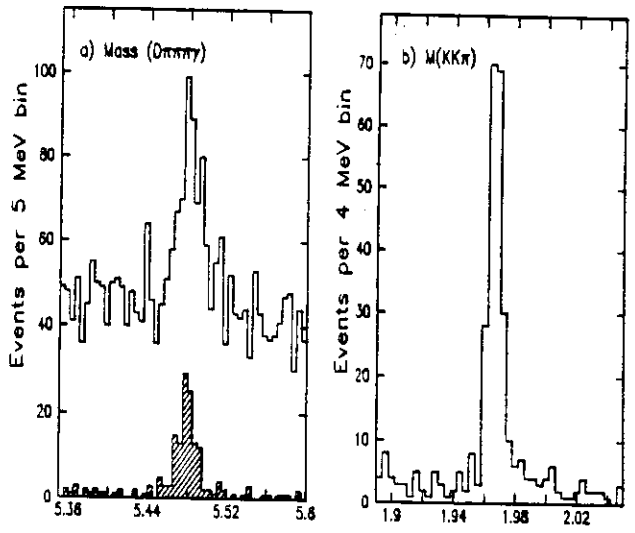

Figure 3: (a) Reconstructed $D^*\pi\pi\pi$ invariant mass and (b) $KK\pi\gamma$ invariant mass. Both plots assume calorimeter energy resolution $\sigma_E/E = 0.5\%/\sqrt{E}$ and position resolution = 0.3 mm. All expected combinatoric background is shown.

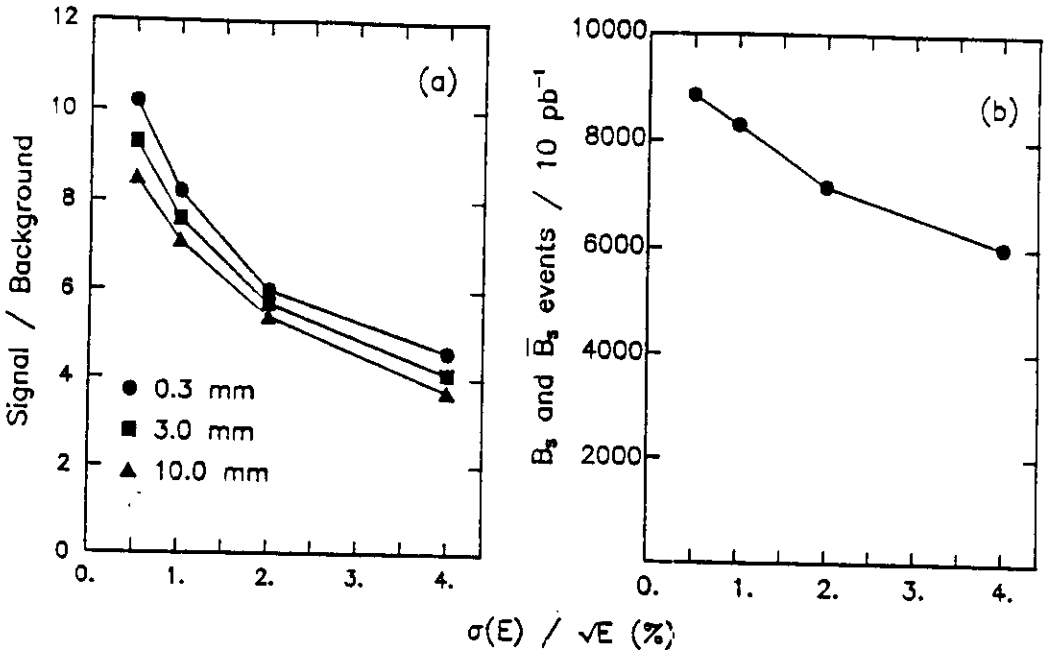

Figure 4: Event yield and Signal/background vs. Calorimeter Resolution: (a) Signal/Background. The dependence is shown vs. k in $\sigma_E/E = k\%/\sqrt{E}$. Curves are given for three different spatial resolutions of the calorimeter. (b) Number of signal events vs. k (for a two arm system).

4. *FLAVOR TAGGING*

4.1 The Use of Muon Tags

In order to understand the tagging possibilities using leptons, we consider two questions, which we then attempt to answer with the use of the Monte-Carlo event generator, PYTHIA 5.1:

1. For events in which a B_s is detected in a 600 mrad spectrometer, what are the momenta and laboratory angles of accompanying leptons? This question is answered in Fig 5, which is a scatter plot of p_μ vs. θ_μ for events containing both an accepted B_s and a muon with at least 1.2 GeV p_t. The expected correlation between μ and B_s is clearly visible. Most muons are in the same hemisphere as the B_s detected at 0° and correlated within ~ 1 unit of rapidity. Furthermore, the muons within the spectrometer aperture of 34.9° (600 mrad) are seen to have much larger momenta than those outside the spectrometer. We conclude that, for detected B_s in the 600 mrad spectrometer, there is not much to be gained by constructing additional lepton detection outside the 600 mrad aperture.

2. What is the momentum and direction of B_s mesons associated with muons detected by a central muon detector, for example the UA1 detector which can identify muons in the pseudorapidity range $|\eta| < 2$ and transverse momentum range $p_{t\mu} > 3$ GeV? This question is answered with reference to Fig. 6, which is a scatter plot of momentum (p_B) vs. laboratory angle

(θ_B) for B_s mesons associated with muons in the above kinematic range. There remains a strong polar preference for the direction of the B_s. Those B_s's with θ_B < 600 mrad have substantially higher momenta than those outside the spectrometer aperture, whose average momentum is less than 10 GeV. The mean flight path for B_s mesons accepted by the spectrometer is ~ 2.5 mm, compared to ~ 0.6 mm for B_s mesons outside the spectrometer. Thus, for optimum triggering, reconstruction and resolution, the B_s's of choice for mixing measurements are those seen by our proposed detector.

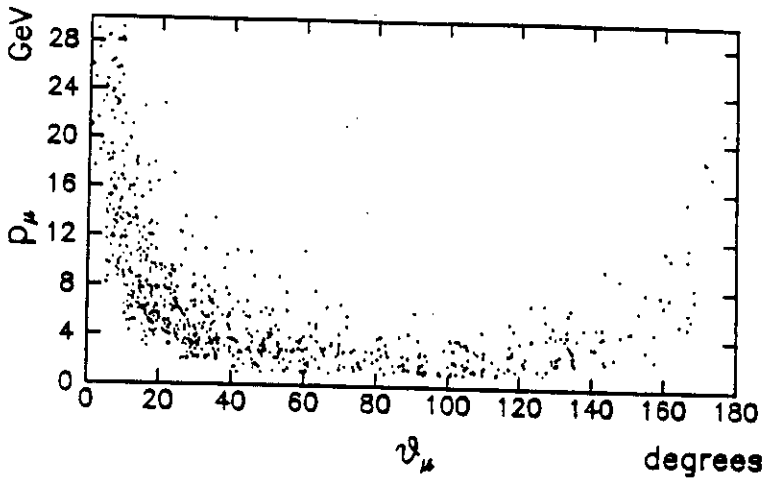

Figure 5: Lab momentum vs. lab angle of muons accompanying an accepted B_s. In this plot, the detected B_s is on the 0° side. Additionally, the muons are required to have p_t > 1.2 GeV.

Some properties of Figs. 5 and 6 are summarized in Table 3, for events in which a B_s meson is fully accepted in the 600 mrad aperture. For each of five different requirements on θ_μ and $p_{t\mu}$, the fraction of tagged B_s mesons is given together with the tagging quality (this is the fraction of those tagged B_s which are tagged by a muon with correct sign). We note here that, following the discussion given in Chapter 2 on mistagging, the contribution to the dilution factor, K, which governs the oscillation amplitude, is given by: (good tags − bad tags)/all tags.

In the first row of Table 3, there are no restrictions on either θ_μ and $p_{t\mu}$. Thus, the fraction tagged (22%) is nearly equal to the semi-leptonic decay probabilities of the second B, both for the b→c transition and the c→s transition (= 11.2% + 6.7%) (the equality is not exact since more than one muon is present in some events). The good/all ratio is 54% for this class of events, indicating that no useful lepton tagging can result from the complete lepton sample without a $p_{t\mu}$ cut (K ~ 0).

Case B, which has a relatively modest $p_{t\mu}$ cut, tends to exclude leptons from charm decay, thereby increasing the percentage of good tags to 81%, but loses ~ 2/3 of the leptons. Case C, which corresponds approximately to the UA1 muon trigger, has a very good tagging efficiency, although only 1.4% of the B_s mesons are tagged (we emphasize that in the generation of these events, we have not "tuned" PYTHIA to agree with UA1 measurements).

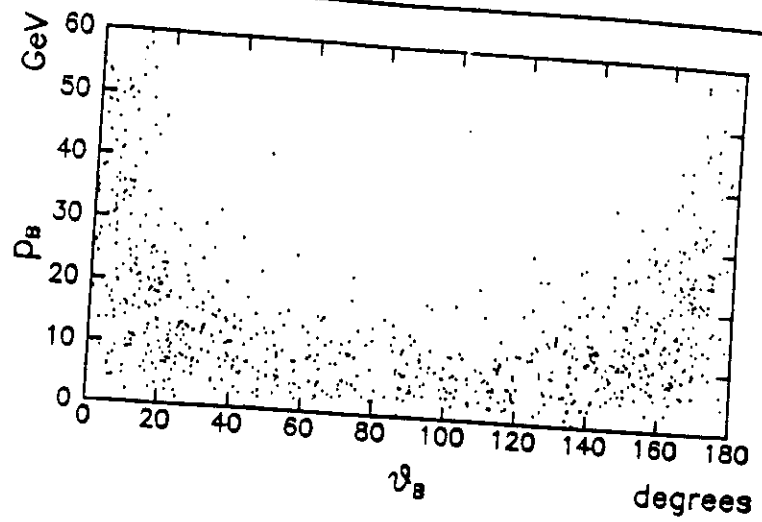

Figure 6: Lab momentum vs. lab angle of B_s mesons for events containing a muon with p_t > 3 GeV and $|\eta| < 2$.

Table 3: Flavor tagging of Accepted B Mesons with Muons(*)*

	Angular Range	pt Range (GeV)	Fraction Tagged	Good/All	Comments
A	all	all	.22	.57	Useless
B	$\|\eta\| < 2$	> 1.2	.061	.81	
C	$\|\eta\| < 2$	> 3.0	.014	.91	"UA1-like" trigger
D	θ < 600mrad	all	.12	.56	Useless
E	θ < 600mrad	> 1.2	.047	.82	Possible with P238

(*) All entries in this table are calculated with PYTHIA 5.1. No attempt was made to tune, for example, the muon p_t distribution with that measured by UA1.

Case D, in which the tagging muon is required to be in the 600 mrad aperture, but in which no selection on $p_{t\mu}$ is made, is useless since the tagging efficiency is ~ 50%, as in case A. If the modest

1.2 GeV $p_{t\mu}$ cut is added (case E), the tagging efficiency increases to an acceptable 83%. The disadvantage of this tagging method is that only 4.7% of the accepted B_s's are tagged.

Although this study considered only muons, both muons and electrons could, in principle, be used as tags. If electron tags were added, the fraction of tags could increase to an upper limit of 9.4% in Case D. However, additional losses arise from Cerenkov limitations and various cuts, needed to minimize the background coming from sources such as pion decay and Dalitz electrons. We have not attempted to estimate these losses since, as discussed in the next section, the use of kaon tags looks more promising and we intend to rely on kaons rather than leptons to tag the B_s flavor.

4.2 The Use of Kaon Tags

We have investigated the possibility of using charged kaons as tags. Our overall strategy is to assign a tag based on the sign of kaons found in the spectrometer and based on whether or not the found kaon tracks, as measured in the vertex detector, point to the primary vertex. We consider below various schemes for handling this information. All calculations are done with PYTHIA 4.7.

There are two major sources of kaons in an event which contains a reconstructed B_s. They either come from the accompanying B meson or they come from the primary vertex. We refer to these as "secondary kaons", K_s, and "primary kaons", K_p, respectively. In general, there is a "good" version and a "bad" version of each. This refers to whether their sign correctly tags the flavor of the produced B_s meson or not.

1. Good K_s: kaons which contain the s-quark at the end of the $b \to c \to s$ chain correctly tag the flavor of the accompanying B-meson at decay.. These kaons will often be measured to be inconsistent with pointing to the primary vertex. However, when the flight path of the accompanying B is too short for this to be the case, the kaon will incorrectly be called a primary kaon and will give a bad tag.

2. Bad K_s: kaons arising from the $W^{\pm}$ in either the $b \to c$ or the $c \to s$ transition can have either sign. Since they will often be measured as being inconsistent with pointing to the primary vertex, they produce a background for the good K_s tags discussed in the first point.

3. Good K_p: these kaons contain the $\bar{s}$-quark which is created in association with the s-quark contained in the B_s meson and can also be used as tags (Note, however, that the sign of these kaons is opposite to those kaons in point 1. Here a $K_p = K^-$ implies a $\bar{B}_s$ meson.) These kaons will in general be produced nearby in rapidity to the reconstructed B_s meson and can be distinguished from the kaons in point 1 since they are produced at the primary vertex. They have an advantage over K_s's from the decay of the accompanying B, in that they suffer no oscillation effects.

4. Bad K_p: kaons produced from the $s\bar{s}$ sea in the numerous hadronization processes at the primary vertex are not associated with the B_s or $\bar{B}_s$ mesons. Such kaons can be of either flavor and thus dilute the kaon tagging. These kaons are particularly troublesome for the tags discussed in point 3 since they are also associated with the primary vertex.

We have studied possible tagging schemes with PYTHIA generated events which contain a B_s meson decaying according to Reaction 10 in Section 3.1. No requirements are made on the hadronization or decay of the associated b-quark. As described in the P238 proposal, events are passed through our trigger simulation software and the B_s is reconstructed. We next sort the kaons, which are accepted by the spectrometer, according to charge and check if the kaon track is consistent with pointing to the primary vertex, using the software simulation package for the micro-vertex detector and online algorithm. Those kaons which are consistent with coming from the primary vertex are K_p; those which are inconsistent are called K_s.

Table 4 contains the results of a study of 313 reconstructed B_s mesons in the form of a matrix. The top row contains events in which no correct tag was found. The second row contains events in which one (or more) good K_s tag is found. The third row contains events in which one (or more) good K_p tag is found. The bottom row contains events which contain both good K_s and K_p tags. Similarly, the first column contains events in which no bad tags are found. The second column contains events with bad K_s tags. The third column contains events with bad K_p tags and the fourth contains events with both bad K_s and K_p tags. Note that, since the event generator program, PYTHIA, contains no B oscillation effects in it, it is possible to know for each event, what constitutes a good tag or a bad tag.

Table 4: *Numbers of Good vs. Bad Kaon Tags in 313 B_s Events**

		Bad tags			
		none	K_s	K_p	both
Good Tags	none	84	18	22	5
	K_s	41	(23)	12	[2]
	K_p	51	1	(18)	[1]
	both	16	[5]	[8]	(6)

(*) Note that events in round brackets, ( ), have one pair (or both) of either K_s^+ and K_s^- or K_p^+ and K_p^-. They provide no tagging information and can be dropped from the table. Events in square brackets, [ ], have in addition to such pairs, also one (or more) K_s or K_p. These events therefore provide unique tags and can be added to the appropriate tagged event samples in the first column or first row.

The reduction of Table 4 is facilitated by the observation that several categories have, as indicated in the footnote in the Table, both secondary K^+ and K^- or both primary K^+ and K^-. These pairs obviously provide no tagging information and can be dropped from further consideration or, if there is an additional K_s or K_p in the event, added to the appropriate first column or first row entry. After these steps, we are left with 12 events in the category, good K_s and bad K_p, and 1 event in the category, bad K_s and good K_p. For these events, a correct tagging statement is clearly made by giving priority to the K_s.

With the steps outlined in the previous paragraph, we are able to form Table 5, which is a list of all uniquely tagged events. There are 3 types, those where the tag is provided by a K_s or K_p, respectively, and those where both both agree. The total number of tagged events is 182 events which is 58% of the total 313 events. All types have approximately the same tagging efficiency, which is 73% for the total sample.

In conclusion, we find that we can use kaons found in the spectrometer to tag more than half of all events containing a reconstructed B_s meson. This is more than a factor of five larger than the best

Table 5: Kaon Tagging Efficiencies

	Events	Fraction Tagged	Good Tags	Bad Tags	Good/All
K_s	81	.26	61	20	.75
K_p	80	.26	56	24	.70
K_s and K_p	21	.07	16	5	.76
Total	182	.58	133	49	.73

we can hope for with a lepton tag. The "trick" which makes this possible is the segregation of primary vertex kaons from kaons originating from secondary vertices by using impact parameter information provided by the silicon vertex detector. Our estimates of the primary tags depend heavily on PYTHIA's hadronization scheme. Nevertheless, our conclusion remains that tagging with kaons is probably much more efficient than tagging with leptons.

5. MEASUREMENT OF B_s LIFETIME

The mean reconstructed B-meson momentum of about 35 GeV/c (see Fig. 6 in P238) and the mean distance of 2 cm between event vertices and first silicon detector plane (see Appendix B in this document) allow rather good measurements of proper flight time for each event.

Fig. 7 displays the simulated proper time distribution (in units of B mean life) expected for the 9000 event total B_s and $\bar{B}_s$ data sample obtainable in a 10 pbarn^{-1} run with a single arm instrumented and using Lead-Glass calorimetry. This distribution shows the fitted curve used for maximum likelihood fits described in the next chapter.

It is seen in Fig. 7 that we have excellent acceptance in t above about one mean life. The departure from a pure exponential in Fig. 7 illustrates the combined effect of the geometrical acceptance (aperture) and trigger efficiency. The acceptance function, $A(t) = 4t^2/(1+4t^2)$, approximately describes the net acceptance and is used in the generation of Monte-Carlo events in the analysis described in Chapter 6. This function is multiplied by $e^{-t/\tau}$ and shown superimposed on the data in Fig. 7. In chapter 6, simultaneous fits to the data shown in Fig. 7 and to the subset which is flavor tagged (see Chapter 5) are performed to obtain the B_s mean life, $x = \Delta M/\Gamma$ and the dilution factor, K.

The experimental resolution in the measured proper time is obtained by comparing the generated B_s flight path with its reconstructed value (see Chapter 7 in P238) for a large number of Monte-Carlo events. This difference quantity is plotted in Fig. 8 and is seen to have a standard deviation, $\sigma_z = 180$ μm. This is an improved version of Fig. 33 on page 54 of P238.

The error in proper time, σ_t, is obtained from the relation $z = ctp/m$ and $\sigma_z = 180$ μm. With a mean $p = 35$ GeV/c, we find $\sigma_t = 6.7$ %. For a number of reasons, the expected value will be somewhat smaller than this. Firstly, the data in Fig. 8 are calculated using a distance of 5 cm between sili-

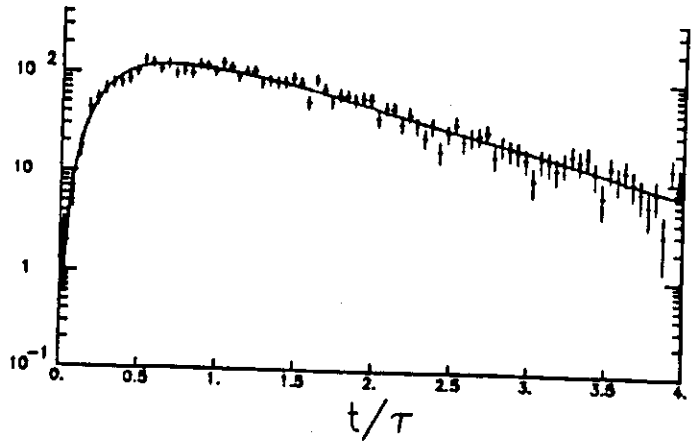

Figure 7: Simulated proper time distribution (in units of B mean life) for 9000 reconstructed B_s events. The departure from a pure exponential illustrates the acceptance effects of geometry, trigger and event reconstruction. The superimposed curve is the empirical acceptance function $A(t) = 4t^2/(1+4t^2)$ multiplied by $e^{-t/\tau}$ This curve is a reasonably good fit to the B events which have been accepted by our trigger simulation and reconstruction programs.

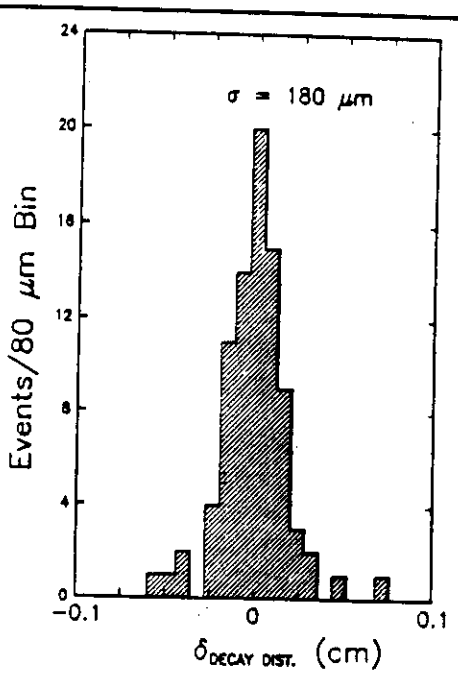

Figure 8: Difference between Monte-Carlo generated and reconstructed B track length. The width of this distribution (standard deviation, $\sigma_z = 180\ \mu m$) gives the uncertainty in our measurement of the B track length. As discussed in the text, several improvements in software and hardware will result in σ_z actually being smaller than this value.

con detector planes used in the P238 silicon configuration. We have since decided to decrease this distance to 4 cm (see Appendix B in this document). Secondly, the algorithm used in the calculation of the data in Fig. 8 can be further improved.

6. SIMULATION AND ANALYSIS OF B_s MIXING

As discussed in the previous chapters, we expect a total sample of at least 9000 fully reconstructed B_s and $\bar{B}_s$ mesons with measured proper decay time, per 10 pbarn^{-1} integrated luminosity if both outgoing arms are instrumented with spectrometers and $0.5\%/\sqrt{E}$ electromagnetic calorimetry is used. This minimum number assumes that only the decay modes listed in Table 2 are reconstructed. The observation of additional decay modes obviously increases the event yield. According to the tagging discussion in Chapter 4, 58% of these events, or about 5000, will be tagged with charged K-mesons.

Six different observable proper time distributions can be formed using these events, as shown in Table 6. The expected numbers of events of each type are also shown, as well as the mathematical function which is to be fit to each.

Table 6: Types of Proper Time Distributions & Sample Sizes[a,b,c]

Type	No. Events	Nature of Proper Time Distribution
B_s untagged	1980	$A(t) \cdot e^{-t/\tau}$
$\bar{B}_s$ untagged	1980	$A(t) \cdot e^{-t/\tau}$
B_s tagged with K^+	1260	$A(t) \cdot e^{-t/\tau} \cdot [1 - K\cos(xt/\tau)]$
$\bar{B}_s$ tagged with K^+	1260	$A(t) \cdot e^{-t/\tau} \cdot [1 + K\cos(xt/\tau)]$
B_s tagged with K^-	1260	$A(t) \cdot e^{-t/\tau} \cdot [1 + K\cos(xt/\tau)]$
$\bar{B}_s$ tagged with K^-	1260	$A(t) \cdot e^{-t/\tau} \cdot [1 - K\cos(xt/\tau)]$

(a) The total number of events in this table, 9000, corresponds to an integrated luminosity of 10 pbarn^{-1} and two instrumented arms, as discussed in Chapter 3. The tagging fractions are discussed in Chapter 4. The equations are derived in Chapter 2.
(b) The sign of the K tag shown in each case assumes it is a secondary K, as explained in Chapter 4. If it is a primary K, its sign must be opposite to correspond to the function shown.
(c) For the tagged distributions, the actual numbers of events will be somewhat different when x is small since the integrals of the two types of functions are not equal.

In these formulae the mixing parameter, $x = \Delta M/\Gamma$ and τ is the B_s lifetime. Thus, the proper time, t, appears in units of this lifetime. K is the "dilution" factor, explained in Chapter 2, which results from all types of "mis-tagging". A(t) is the acceptance factor which depends on trigger efficiency and event reconstruction efficiency, as discussed in the last chapter.

In order to demonstrate the expected statistical significance in the determination of x, τ and K with samples of this size, and also to show how the significance depends on sample size and background, we have generated Monte-Carlo data samples and subjected them to joint maximum likelihood fits with x, τ and K as free parameters. In the generation, the acceptance function is taken to be $A(t) = 4t^2/(1+4t^2)$. As explained in Chapter 4, this curve describes the simulated data sufficiently well for our present purposes.

A Monte-Carlo data sample of 9000 events was generated according to the equations listed in Table 6 for each of the x values, 0.7, 5, 10 and 15. The value of K used in the generation was fixed at 0.34, which is approximately the product of the dilution factors discussed in chapters 2 and 4, but also includes a factor of 0.95 for Cerenkov misidentification and takes into account the fact mentioned in Chapter 4 that oscillation of the tagging particle is not a relevant concern for K_p tags.

A simultaneous maximum likelihood fit was then made to the entire data sample using, for each event, the relevant equation. For example, the likelihood function for a B_s tagged with a "secondary" K^+ is:

$$\mathcal{L} = \frac{A(t) \cdot e^{-t/\tau} \cdot [1 - K\cos(xt/\tau)]}{\int A(t) \cdot e^{-t/\tau} \cdot [1 - K\cos(xt/\tau)]\, dt}$$

The sum of $-\log \mathcal{L}$ for all events is minimized using the program MINUIT. The results are shown in Figs. 9 for all four values of x and the fitted parameters K and x are given in Table 7.

A measure of the uniqueness of the maxima found in the likelihood function is given by plotting, for each case, the value of that function vs. x, with fixed τ and K. τ can be obtained independently from the time distribution of the entire sample and the value of K is known reasonably well from physics arguments and observed background. Such plots are shown in Fig. 10.

The fits shown in Fig. 9 and Table 7 are excellent. The fluctuations in the likelihood function vs. x seen in Fig. 10 are a very small fraction of the convergence peaks. We can thus conclude that, if our estimates are correct, a successful experiment could be performed with far fewer events and/or more background.

Thus, we now investigate the dependence of the quality of the results on sample size and background. This will allow us to finally decide on (a) whether to instrument only one arm or both arms; (b) whether to construct a Lead-Glass calorimeter or a Liquid-Xenon calorimeter.

The parameters which best indicate the sample size required for a good measurement of B_s mixing are the error in the mixing parameter (σ_x) and the significance of the oscillation amplitude (N_σ = K divided by the error in K). We plot these two quantities as a function of the number of signal events in Fig. 11 for a fixed K value of 0.34 and an x value of 15. It can be seen from this figure that at the expected yield of 3000 events for a Lead-Glass calorimeter and one instrumented arm, we expect a highly significant measurement (9 standard deviations in the oscillation amplitude) and an error of less than ± 0.1 on the measurement of x.

This is further illustrated in Fig. 12 which show the results of likelihood fits performed on a sample size of 3000 simulated events for the same x values used in Fig. 9. In the simulation of this 3000 event sample, we have also taken into account the expected signal/background ratio (about 4 for the Lead-Glass calorimeter) illustrated in Fig. 4 of section 3.2. Since the background is mainly associated with B events, we assume that it will have an exponential proper time dependence with the same lifetime as the signal. With this assumption, the only effect of the background is to dilute the oscillation amplitude and thus reduce K. Even with this additional dilution, the significance of the measurement is still good and the error on x is everywhere less than ± 0.1.

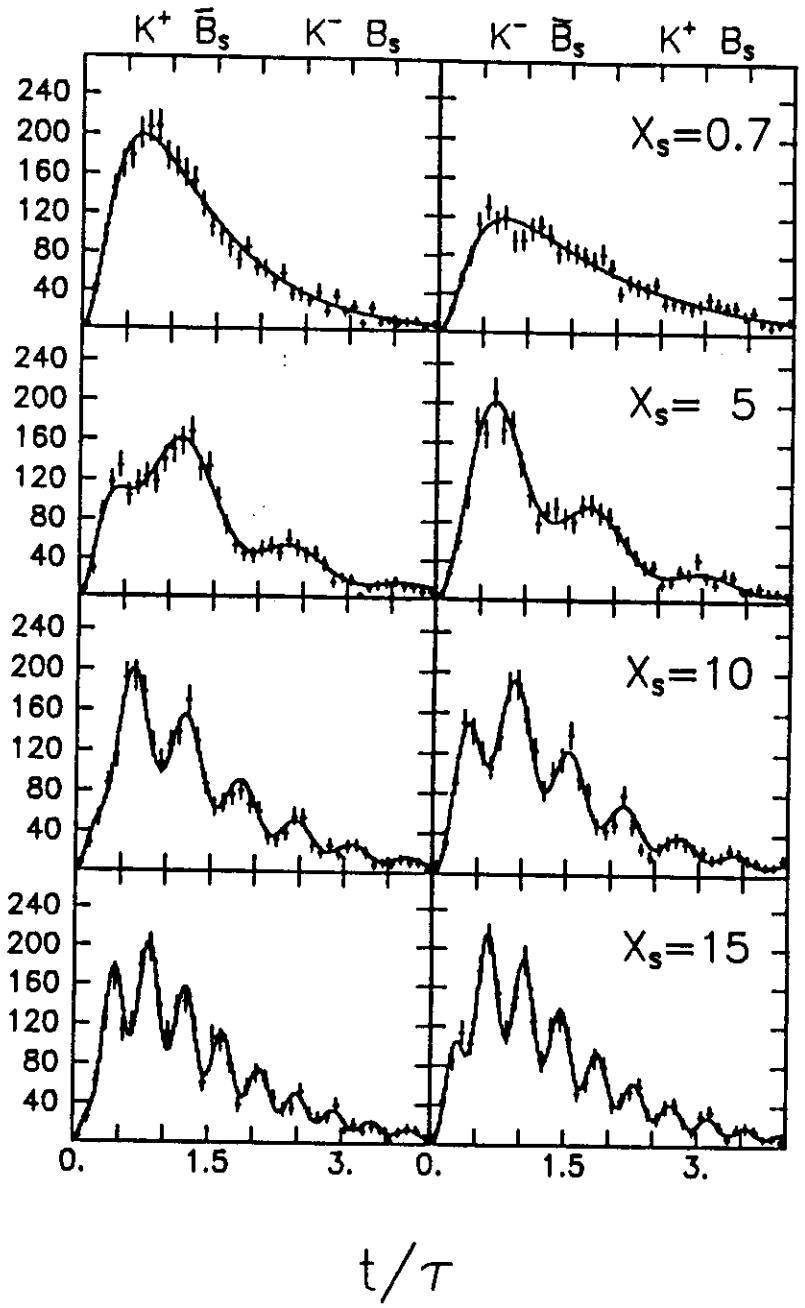

Figure 9: Proper time distributions for the two types of tagged events shown in Table 6 (a,b) x = 0.7, (c,d) x = 5, (e,f) x = 10, (g,h) x = 15. The Monte-Carlo data points correspond to a total sample of 9000 events as discussed in the text. The curves result from simultaneous maximum likelihood fits to the data shown and the proper time distribution of the entire 9000 event sample.

Table 7: *Parameters Obtained From Fits[a] Shown In Fig. 9*

Input x Value	Fitted K	Fitted x
0.7	0.27 ± 0.03	0.70 ± 0.05
5.0	0.30 ± 0.02	4.99 ± 0.03
10.0	0.32 ± 0.02	9.96 ± 0.03
15.0	0.33 ± 0.02	14.93 ± 0.03

(a) For a 9000 event sample

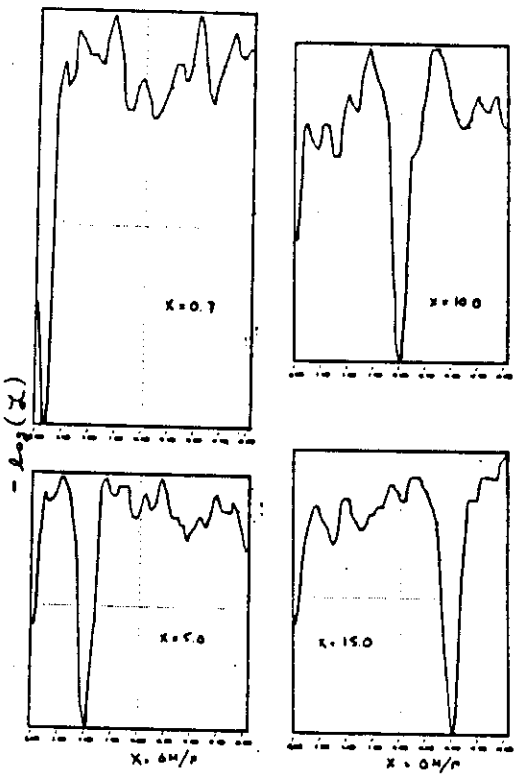

Figure 10: The log-likelihood function plotted vs. the mixing parameter, x for four data samples generated with x = 0.7(a), 5(b), 10(c), 15(d). The values of τ and K are fixed to their generated values.

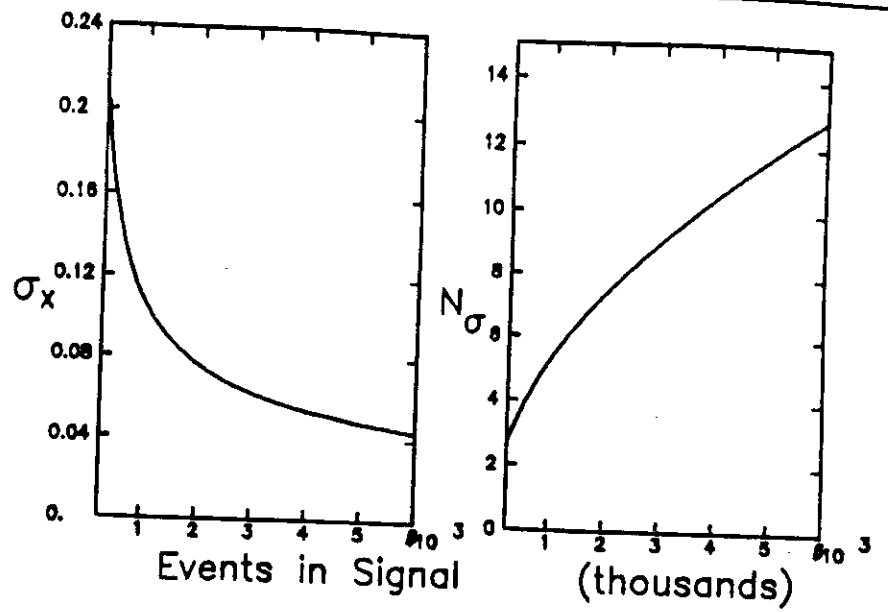

Figure 11: (a) Error on the mixing parameter (σ_χ) vs. the number of B_s signal events. (b) The significance (in standard deviations) of the oscillation amplitude (K) vs. the number of B_s signal events.

The 3000 event sample obtained when we assume one instrumented arm and a Lead-Glass calorimeter, is seen to yield an acceptably precise and significant measurement of the mixing parameter x. We next try to find the minimum event sample size which will allow an adequate measurement of the mixing parameter. Refering again to Fig. 11, we see that a sample size of as few as 500 events will give a 4σ measurement and an error on x of about 14%. We investigated the uniqueness of the solution by studying (as in Fig. 10) the log-likelihood function vs. x for several randomly generated samples for each type of sample size. In Fig. 13(b), we show a typical example of the resulting curves. In Fig. 13(a) a typical (bad) example of the result for a 250 event sample shows that it is not possible to obtain reliable results with such a small sample. For comparison, Figs. 13(b,c,d) show typical log-likelihood functions plotted vs. x for sample sizes of 500, 1000 and 3000 events, respectively. We conclude that a sample size of 500 events is the smallest sample size from which a meaningful result could be obtained. Thus, our prediction of 3000 events implies a safety margin of about a factor of six.

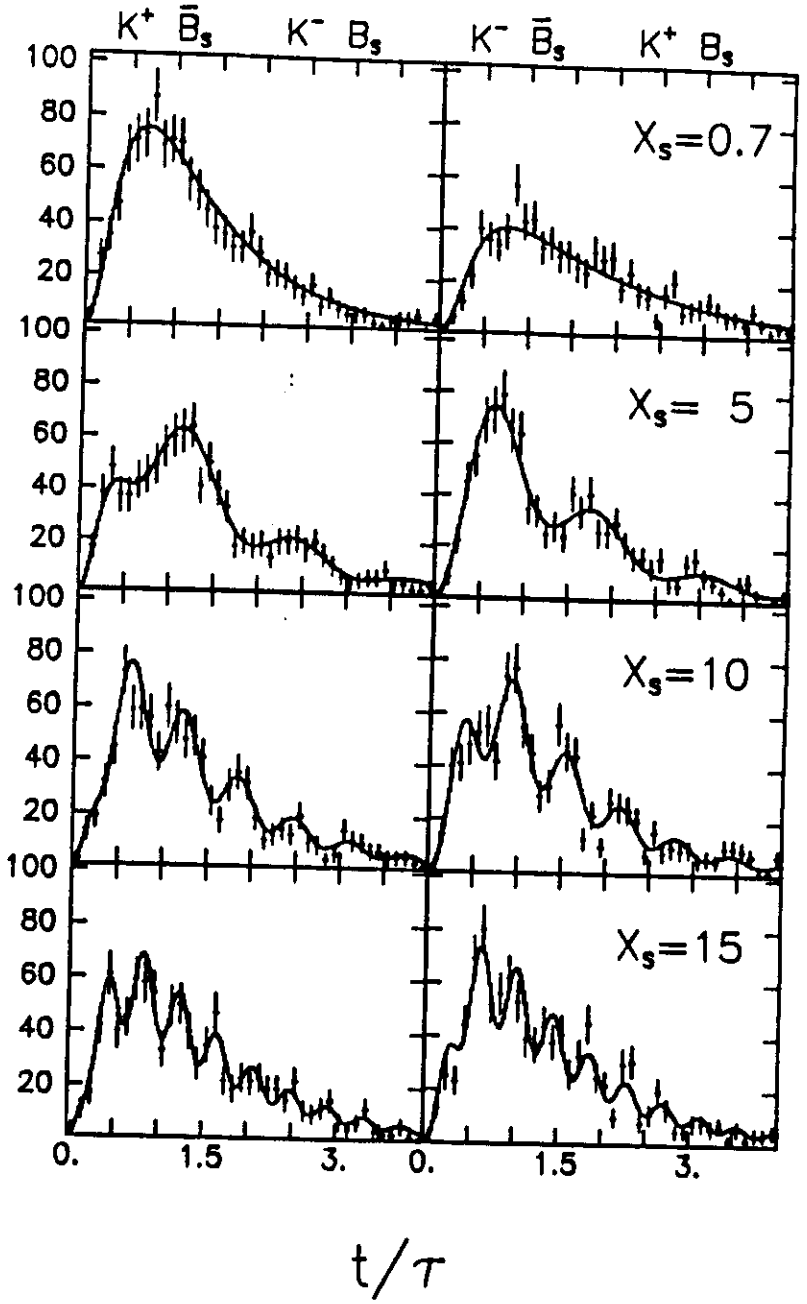

Figure 12: Proper time distributions for the two types of tagged events shown in Table 6 (a,b) x = 0.7, (c,d) x = 5, (e,f) x = 10, (g,h) x = 15. The Monte-Carlo data points correspond to a total sample of 3000 events as discussed in the text. The curves result from simultaneous maximum likelihood fits to the data shown and the proper time distribution of the entire 3000 event sample.

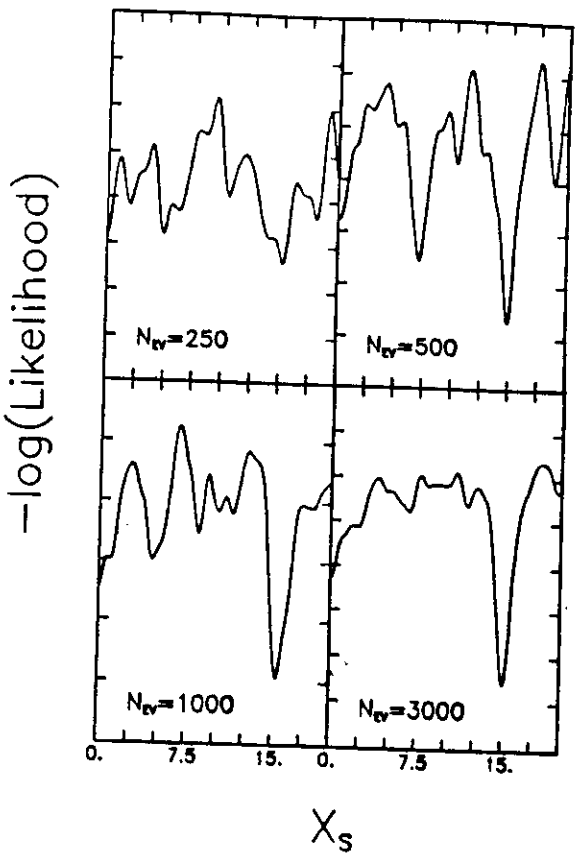

Figure 13: $-$*Log-Likelihood Function vs. x: The data samples of* 250, 500, 1000 and 3000 events were all generated with x = 15. In each case, the distributions are typical examples from a study of 20 Monte-Carlo experiments.

7. OVERVIEW OF OTHER EXPERIMENTS

We have been asked to compare this experiment with other experiments which will take data in the next few years, with regards to the feasibility of measuring the B_s mixing parameter. This is a hard task since, to our knowledge, no detailed analysis of the type presented in this addendum to P238 exists for the other experiments. Some work along these lines has been done to evaluate the impact of new or upgraded machines (see for example Roudeau [Selected topics in B physics at LEP, LAL 89$-$21] on B_s mixing at the luminosity-upgraded LEP).

We limit ourselves, therefore, to give a table of indicators (Table 9) which is meant to provide a qualitative understanding of the relative merits of different experiments.

The choice of indicators is based on the fact that the determination of x_s requires a precise measurement of the time distribution of B_s and $\bar{B}_s$ (where the particle / antiparticle identity is defined at $t = 0$). The figures of merit are:

1. The expected number of tagged B_s ($\bar{B}_s$) mesons selected by the trigger which have all the decay products within the detector acceptance.

2. The capability of fully reconstructing B_s final states, a characteristic that depends crucially on the quality of particle identification, especially π-K separation.

3. The precision of the reconstruction of the vertex coordinate. Vertex measurement is essential both as a tool for identifying secondary vertices, and to measure the time distribution accurately.

We have chosen four experiments to represent general classes of experiments (e^+e^- low energy collider, fixed target, etc.). In our opinion the chosen experiments have the highest sensitivity to B_s of experiments in their respective classes. We do not consider experiments to be done at machines that either are in the design stage (PSI, SSC, etc.) or require major upgrades (High Intensity LEP, Fermilab Tevatron with a new main injector) since they will take place, we trust, on a different time scale.

The estimates for the number of events from the different experiments is straightforward. The number of $B_s + \bar{B}_s$ is equal to

$$2 \cdot \int \mathcal{L}\, dt \cdot \sigma_{b\bar{b}} \cdot F_s \cdot A$$

where F_s is the number of B_s (or $\bar{B}_s$) per $b\bar{b}$ event, and A is the fraction of B_s or $\bar{B}_s$ events with the decay products in the spectrometer. We have used the input values described in Table 8. Where detailed information is not available, a reasonable upper limit is used.

Table 8: Estimates of event samples

Experiment	CLEO (Υ5S) (CESR)	DELPHI (LEP)	E771 (FNAL)	CDF (FNAL)	P238
Integrated $\mathcal{L}$	10^3 pb^{-1}	150 pb^{-1}	250 pb^{-1}	10 pb^{-1}	10 pb^{-1}
σ_{bb}	0.27 nb	6.5 nb	20 nb	45 μb	10 μb
B_s Fraction (F_s)	1.0	0.2	0.2	0.2	0.2
Acceptance (A)	1.0	1.0	1.0	1.0	0.295
Number[1] of B_s in Detector	5.4×10^5	3.9×10^5	2×10^6	1.8×10^8	1.2×10^7

[1] Per run of 10^7 sec. of data taking

We repeat the last row of Table 8 (the estimate of the number of B_s events in each detector) at the top of Table 9. The second row of this table gives the expected yield after triggering. For the trigger efficiency we have taken arbitrarily $\epsilon_t = 0.8$ for DELPHI and CLEO. For E771, the trigger requires two muons in the final state, and should detect events with one $J/\psi \to \mu^+\mu^-$, or events in which both B's decay semileptonically. The geometric acceptance for the two muons is 0.25. We then take:

$$\epsilon_t = 0.25\cdot[BR(B\to\mu)^2 + BR(B_s\to J/\psi)\cdot BR(J/\psi\to\mu\mu)] = 0.25\cdot[.124^2 + 5\times10^{-3}] = 5\times10^{-3}.$$

For CDF the trigger requires one muon with high p_t so the trigger acceptance is $\epsilon_t = 0.124 \cdot \epsilon_{ptcut}$. Because the minimum p_t is unknown, we leave $\epsilon_{ptcut} = 1$.

The numbers in parentheses in the last line of the table are obtained by multiplying the number of events collected by the trigger by the reconstruction factor obtained for our experiment ($9000/5\times 10^6 = 1.8\times 10^{-3}$). In the case of LEP, this estimate agrees well with the number obtained by scaling down Roudeau's estimate to the nominal LEP luminosity.

Table 9: Comparison of Existing Experiments with P238

	Low Energy e^+e^- Colliders	High Energy e^+e^- Colliders	Fixed Target	$\bar{p}-p$ Colliders	This Experiment
Experiment	CLEO (T5S) (CESR)	DELPHI (LEP)	E771 (FNAL)	CDF (FNAL)	
Number[1] of B_s in Detector	5.4×10^5	3.9×10^5	2×10^6	1.8×10^8	1.2×10^7
$B_s + \bar{B}_s$ Selected by Trigger	4.3×10^5	3.1×10^5	10^4	2.2×10^7	5×10^6
σ_L/L	> .50	.11	.05	.04	< .06
Particle ID	Partial	Yes	Yes?	No	Yes
Event Sample	?	245(558)	(18)	?	9×10^3

[1] Per run of 10^7 sec. of data taking

We conclude that:

1. CLEO is not competitive in this measurement because the decay path is measured very poorly and the sample size is low.

2. CDF is the only experiment which starts out with large statistics, but reconstruction and positive identification of the B_s will be made very difficult by the lack of good quality particle identification.

3. E771 does not have sufficient statistical power.

4. DELPHI is the experiment which comes closest to performing an x_s measurement, but it is still too weak from the statistical point of view. In fact, Roudeau estimates that one needs thirty times the statistics of a typical run to measure this effect.

APPENDIX A: Comments on Data-Driven Processor

As reported in our memo to the committee (SPSC/M 443) of 16 May, 1989, we have decided to use the existing Nevis/University of Massachusetts processor design to implement the trigger algorithm described in the P238 proposal.

We have discussed the P238 algorithm at some length with Bruce Knapp and have realized that the problems we face are simpler than those already solved by the Nevis group for their trigger in Fermilab Experiment E690. There are several reasons for this:

- We look only for straight lines in 3 planes, while they are reconstructing 5 point tracks in an inhomogeneous magnetic field.
- Our algorithm does not call for matching tracks between views. Theirs does.
- We do not require track fitting for parameter estimation. They do.
- Unlike E690, we are not attempting full efficiency for track finding (we would in fact rather lose the low momentum tracks since they have poor impact parameter resolution).
- Since our detector is divided into four independent quadrants and since, at the collider, the tracks are not folded into the forward direction by a Lorentz boost, we have a substantially smaller track density and thus a smaller number of hit combinations to sort through (despite the increased track multiplicity at the collider).

Although they do not try to find an event vertex using all the found tracks in an event, it appears we can adapt and extend techniques they use for track fitting to the vertex finding problem with rather little difficulty.

Fig. 14 is a preliminary block diagram of a processor suitable for the P238 algorithm as described in Section 4.3 of the P238 proposal. We divide the processor into 5 subroutines, which are isolated from each other by control buffers. The 3-plane line finder contains most of the hardware, approximately 160 existing Nevis modules divided into eight identical sections (4 quadrants × 2 views) and is essentially a copy of a basic line-finding subroutine designed by Bruce Knapp et al.

The Nevis processor modules are themselves quite simple. Each module takes one or two 24 bit (16 data + 8 control) input data words, performs some simple operation on them and produces an output which is passed on to the next module. All modules in the system are clocked synchronously and the input and output data words are latched into registers on each clock cycle. Care has also been taken to allow access to all of the input and output registers in the system, either for reading data or inserting data. This greatly simplifies the task of debugging and diagnosing problems since the state of the system can be determined and checked on a cycle by cycle basis.

The rest of the subroutines for the P238 algorithm have not yet been mapped out in complete detail but preliminary design work indicates that we will need fewer than 100 modules for the rest of the system (for a total of about 260 modules compared to about 700 modules for the E690 processor). We will need to design one module for the Histogrammer subroutine but can probably use existing Nevis modules otherwise (although perhaps some minor modifications may be necessary). Detailed design of the system awaits the completion of the software emulator package (described below).

The processor emulator is a software package designed to simulate the action of the processor on a cycle by cycle basis. Each processor board type (of which there are 47) is simulated by a separate subroutine. The simulation extends not only to the processing of event data but also communication with the processor control structure. The emulator can thus mimic such actions as the loading of tables, the processing of real data, or loading and reading test data words into any register in the system.

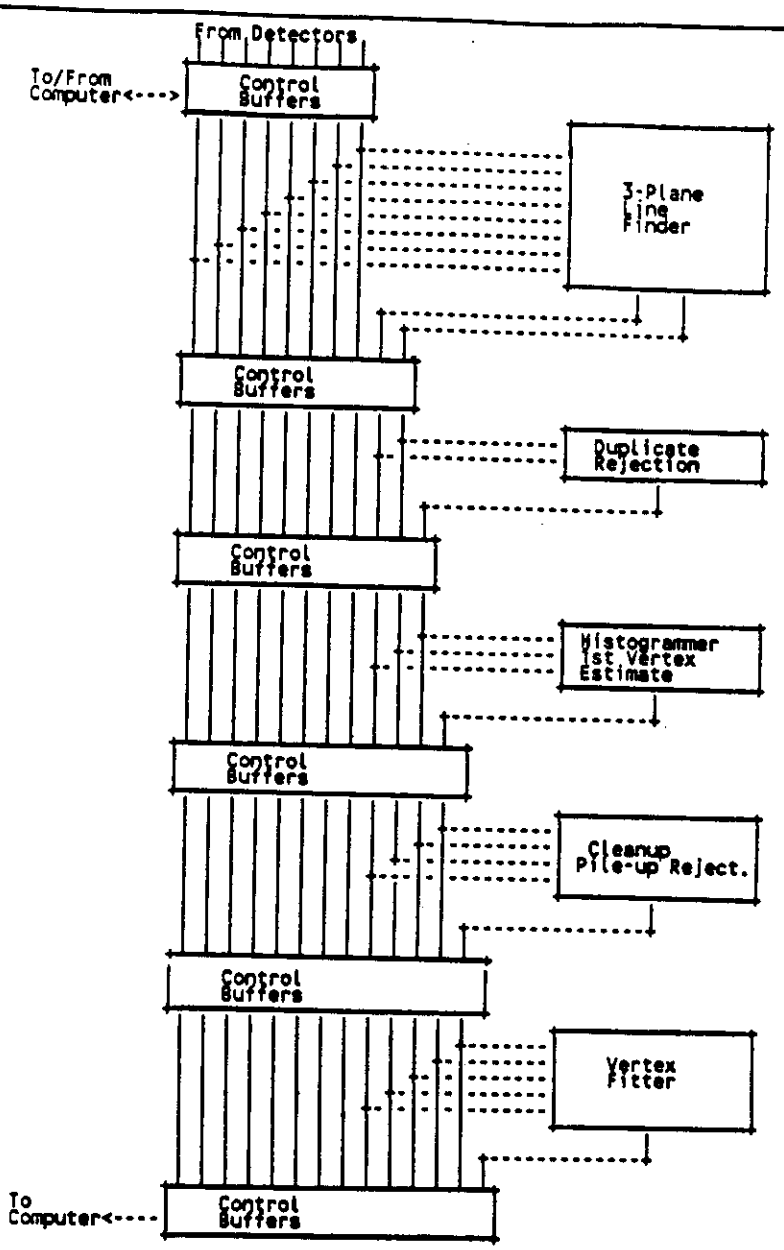

Figure 14: Preliminary block diagram of P238 processor

A processor algorithm consists of a list of boards, the specification of the contents of any memory elements on those boards and the specification of how these boards are to be cabled together. Such a list is known as a configuration file. The emulator reads this file in its initialization phase and thus determines which board subroutines must be called. It calls these subroutines which in turn reserve enough memory to hold any tables which must be downloaded as well as memory locations for the input and output registers. Storage is also reserved to hold cable contents and pointers are set up to the memory locations which hold the contents of the input and output cables. After this initialization phase, the memory locations reserved to hold on-board tables are loaded by simulating the cycles that would be executed by the processor hardware in performing this function.

At this point, the emulator is ready to process data. Data is put into the locations reserved for input cables and the board subroutines are called for each board listed in the configuration file. Each board subroutine checks for data on the input cables, and if present performs its operation and modifies the memory locations reserved for its on-board registers as well as that reserved for its output (and possibly input) cable. This procedure completely emulates the processing performed in one clock cycle. It can then be repeated any number of times to simulate subsequent cycles. If the process is repeated a sufficient number of times, the data will eventually propagate through the entire "processor" (assuming it is correctly designed) and start appearing in the locations reserved for the output control buffers, together with the processed data.

Using the emulator, it will be possible to precisely predict the operation of a given algorithm on any set of simulated event data. For example, the average number of clock cycles per event can be easily determined and problems of precision can be investigated.

The emulator will be usable not only for the design and evaluation of processor configurations but also for diagnostics since the same data can be given to both the emulator and the real processor and the results of the computation compared. The operation of a single board can thus be evaluated as can the operation of an entire subroutine.

We are currently collaborating with E. Hartouni of the University of Massachusetts, Amherst to write this emulation package. Two of us (M. Medinnis and R. Dzhelyadin) are actively writing new modules and debugging existing ones. We are also training a student (D. Lynn)) and plan that before the end of August, to have a team of 4 nearly full-time people (also including J. Zweizig) working on software development at CERN, in addition to E. Hartouni.

Currently, a total of 10 of the required 47 software modules either exist or are under development. We plan to finish writing the code by the end of September or early October. Soon thereafter, some of us will go to Fermilab to work with the E690 collaboration on the installation and debugging of their processor.

Replication of the modules necessary for construction of the processor should be completed by early January 1990. The Nevis / University of Massechusetts collaboration (E690) has agreed to lend us the rack and crates necessary to house a processor of the size we envision.

APPENDIX B: New Silicon Micro-Vertex Detector Configuration

In our simulation work (including that presented in this addendum), we assume a vertex detector consisting of 11 parallel planes, spaced 6 cm apart, with each plane divided into four 7×7 cm^2 silicon squares (see section 4.1 of the P238 proposal). The silicon planes are assumed to be 200 μm thick and to have 25 μm strips on both sides.

After discussions with manufacturers, we have come to realize that such a scheme is not feasible primarily because the 7×7 cm^2 size is too large to comfortably fit on the standard 4 inch diameter silicon wafers. We have thus revised our detector design. We are now considering a detector which consists of sixteen parallel 10×10 cm^2 detector planes divided into four 5×5 cm^2 squares, spaced 4 cm apart. The detector is otherwise the same as that presented in the proposal.

This new configuration results in somewhat improved impact parameter resolution for low momentum tracks which will in turn result in a somewhat improved minimum bias rejection. (We have not estimated the improvement but we do not expect a dramatic effect.) Another advantage of the new design is that it extends the coverage of the interaction region from ± 18 cm to ± 22 cm, thus increasing the fraction of usable events from 81% to 94%. The disadvantage of the new scheme is that the amount of material in the detector increases by 45%. The resulting increase in multiple scattering will not cause problems for the trigger algorithm since only the two planes closest to the vertex are used to estimate track parameters. The effect of increased photon conversions, delta ray production and nuclear interactions has not been simulated, but we do not expect the trigger suppression estimates to change significantly since these processes had but small effect on the original estimates.